

Die Grenzen der Chemie neu ausloten? It takes #HumanChemistry

Wir suchen kreative Chemikerinnen und Chemiker, die mit uns gemeinsam neue Wege gehen wollen – mit Fachwissen, Unternehmertum und Kreativität für innovative Lösungen. Informieren Sie sich unter:

evonik.de/karriere

EVONIK
Leading Beyond Chemistry

Check for updates

Accepted Article

Tissue-like Optoelectronic Neural Interface Enabled by PEDOT:PSS Hydrogel for Cardiac and Neural Stimulation

Mertcan Han[1,γ], Erdost Yildiz[2,γ], Hümeyra Nur Kaleli[2], Selcan Karaz[3], Guncem Ozgun Eren[4], Itir Bakis Dogru-Yuksel[1], Erkan Senses[3], Afsun Şahin[2,5] & Sedat Nizamoglu[1,4,]*

[1]Department of Electrical and Electronics Engineering, Koç University, Istanbul 34450, Turkey

[2]Koç University Research Center for Translational Medicine, Koç University, Istanbul 34450, Turkey

[3]Department of Chemical and Biological Engineering, Koç University, Istanbul 34450, Turkey

[4]Graduate School of Biomedical Science and Engineering, Koç University, Istanbul 34450, Turkey

[5]Department of Ophthalmology, Medical School Koç University, Istanbul 34450, Turkey

[γ]Present address: Physical Intelligence Department, Max Planck Institute for Intelligent Systems, 70569 Stuttgart, Germany

[*]Corresponding Author: snizamoglu@ku.edu.tr

Keywords: Biointerface, hydrogel, cell stimulation, optoelectronic, bioelectronic, neuromodulation, cardiac stimulation

This article has been accepted for publication and undergone full peer review but has not been through the copyediting, typesetting, pagination and proofreading process, which may lead to differences between this version and the Version of Record. Please cite this article as doi: 10.1002/adhm.202102160.

This article is protected by copyright. All rights reserved.

Accepted Article

Abstract

Optoelectronic biointerfaces have made a significant impact on modern science and technology from understanding the mechanisms of the neurotransmission to the recovery of the vision for blinds. They were based on the cell interfaces made of organic or inorganic materials such as silicon, graphene, oxides, quantum dots and π-conjugated polymers, which are dry and stiff unlike a cell/tissue environment. On the other side, wet and soft hydrogels have recently been started to attract significant attention for bioelectronics because of its high-level tissue-matching biomechanics and biocompatibility. However, it is challenging to obtain optimal opto-bioelectronic devices by using hydrogels requiring device, heterojunction and hydrogel engineering. Here, an optoelectronic biointerface integrated with a poly(3,4-ethylenedioxythiophene):poly(styrene sulfonate) (PEDOT:PSS) hydrogel that simultaneously achieves efficient, flexible, stable, biocompatible, and safe photostimulation of cells is demonstrated. Beside their interfacial tissue-like biomechanics, ~34 kPa, and high-level biocompatibility, hydrogel-integration facilitated an increase of charge injection amounts 7-folds with an improved responsivity of 156 mA/W, stability under mechanical bending cycles, and functional lifetime over 3 years. Finally, these devices enable stimulation of individual hippocampal neurons and photocontrol of beating frequency of cardiac myocytes via safe charge-balanced capacitive currents. Therefore, hydrogel-enabled optoelectronic biointerfaces hold great promise for next-generation wireless neural and cardiac implants.

This article is protected by copyright. All rights reserved.

Accepted Article

INTRODUCTION

Cell stimulation is the fundamental mechanism enabling vital functions from senses, such as touch, hear and see, to secretion of hormones and enzymes for regulation of metabolism and homeostasis. Because of that, artificial cell stimulation is a useful tool to understand and investigate biomolecular dynamics in cells and treat a wide variety of neurological disorders.[1] For artificial cell stimulation, light provides a non-invasive, localized, and wireless communication trigger. Light-induced cell stimulation can be achieved by direct use of near-infrared light (e.g. INS),[2] optogenetics,[3] or optoelectronic neural interfaces.[4,5] Thanks to the rise of the bioelectronic medicine, the latter gained considerable attention owing to its nongenetic nature and reduced interference with the cellular integrity. They use the photovoltaic effect to convert light energy to ionic currents for cell stimulation and they are generally made of materials such as silicon,[6–8] graphene,[9] carbon nanotubes,[10] organic dyes[11] and polymers,[4,12–18] nanoparticles,[19,20] and semiconductor nanoparticles[21–25], which are dry and hard. By considering the distinct mechanics and composition of water-rich tissue environments incorporating mobile ions and biomolecules, tissue-like materials can alternatively blur the distinction between the cellular and device interfaces for next-generation human-machine interfaces.

Hydrogels, which has been widely used for cell scaffolds in tissue engineering, started to attract significant attention for bioelectronics.[26] They have unique tissue-like wet and soft characteristics that can match well with the mechanical properties of tissues. While conventional electrode materials

This article is protected by copyright. All rights reserved.

Accepted Article

have Young's moduli in GPas range, hydrogels can have it around on the order of kPas overlapping close to the cell and tissue properties, which can significantly suppress the mechanical mismatch between tissue and device and possible foreign body response by glial cells.[27] Moreover, their conductivity can be tuned by varying the electronic, ionic, or hybrid networks and biodegradability can be introduced by adding cleavable chains.[28] Because of these favorable properties they have been used for bioelectronic systems such as epidermal electrodes and bioartificial skin replacements.[29,30] For optical stimulation of cells, they are used as an optical fiber encapsulating optogenetically-encoded cell lines for sensing and stimulation.[31] However, their utilization for wireless optoelectronic neural interfaces remained unexplored.[32] Even though hydrogels allow for high-level biomechanical match and biocompatibility with cells, since its direct additive integration may result in sub-optimal performance levels,[27] its use is challenging for effective photostimulation of neurons.

In this study, we developed an efficient, flexible and robust hydrogel-integrated optoelectronic neural interface (Fig. 1a). For that we selected poly(3,4-ethylenedioxythiophene):poly(styrene sulfonate) (PEDOT:PSS) as the soft and conductive hydrogel material (Fig. 1b) that match with the band alignment of the photovoltaic unit efficiently directing photogenerated holes to the hydrogel for capacitive charge-transfer at the electrode-electrolyte interface (Fig. 1c-d). As the conducting polymer PEDOT:PSS offers high stability, solution processability, and biocompatibility, it gained significant attention particularly in wearable and organic electronics and hydrogel bioelectronics.[27] The hydrogel composition is engineered by co-solvents and conductivity enhancers for optimal device performance in terms of total charge injection with suppressed faradaic effects. Beside the improved efficiency and tissue-like interface with Young's modulus of ~34 kPa and high biocompatibility, the neural interface shows flexibility (Fig. 1e) and robust operation without mechanical and electrical failures after thousands of cycles bending and accelerated aging test. As proof-of-principle, we tested

This article is protected by copyright. All rights reserved.

Accepted Article

the biointerface on primary neurons and cardiac myocytes isolated from Wistar Albino rat embryos. The device enables stimulation of primary hippocampal neurons under low light intensities below the ocular safety limits. Moreover, it achieved light-triggered control of beating frequency of cardiac myocytes via charge-balanced capacitive currents.

This article is protected by copyright. All rights reserved.

Accepted Article

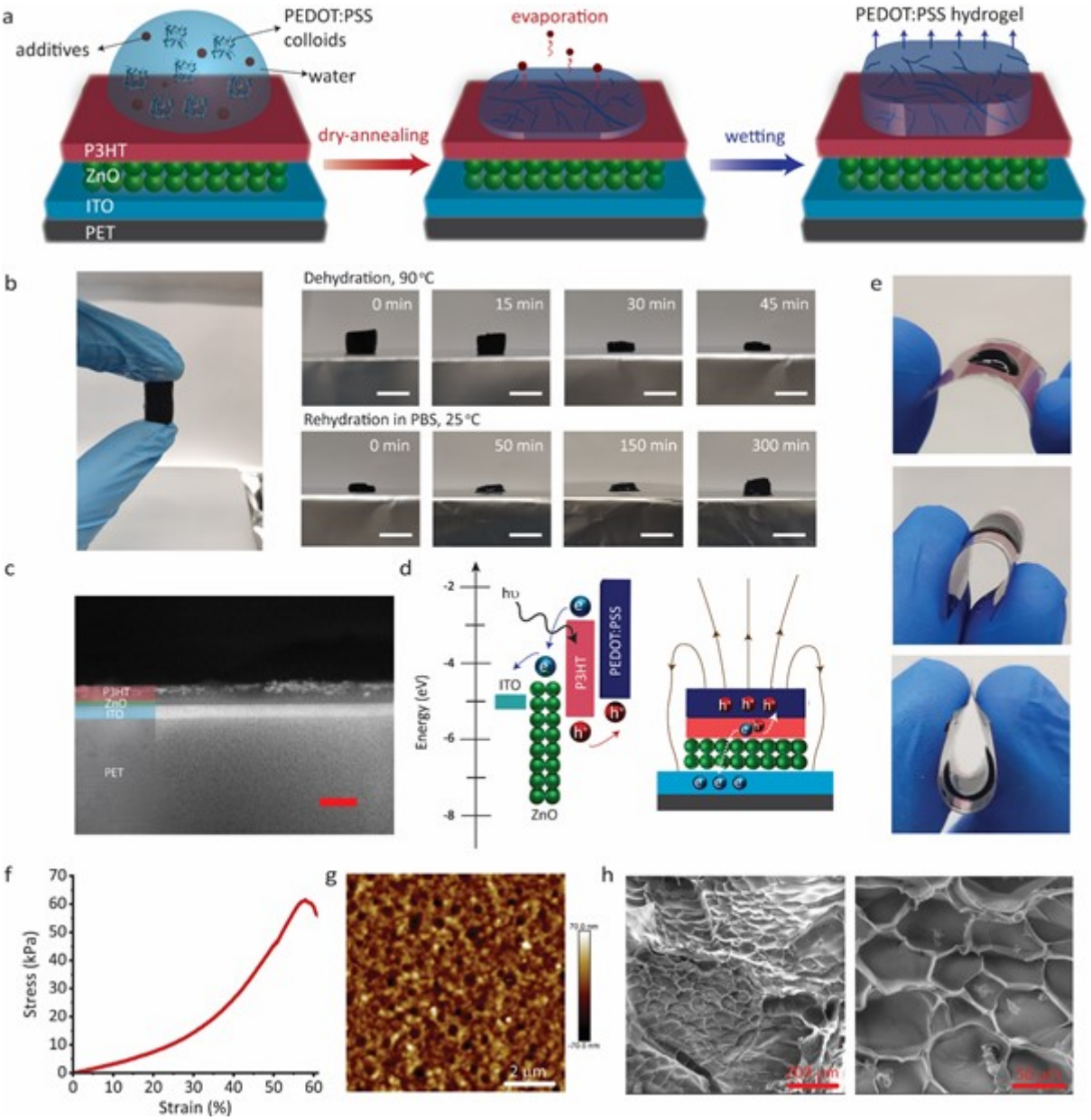


Fig. 1. a Fabrication procedure of the hydrogel-integrated optoelectronic biointerface. **b** (Left) Photograph of the PEDOT:PSS hydrogel. (Right) Photographs of the hydrogel during dehydration and rehydration at different times (scale bar: 10 mm). **c** Cross-section scanning electron micrograph of the biointerface before hydrogel coating (scale bar: 200 nm). **d** (Left) Energy levels of ZnO, P3HT and PEDOT:PSS hydrogel. After the light absorption, the photogenerated electrons and holes are transferred to the ITO and PEDOT:PSS, respectively. (Right) The photogenerated charges will induce

This article is protected by copyright. All rights reserved.

Accepted Article

capacitive current that will return to back to the ITO. **e** Photographs of the flexible hydrogel-integrated optoelectronic biointerface. **f** Stress-strain behavior of PEDOT:PSS hydrogel. **g** AFM surface height profile of PEDOT:PSS hydrogel coated biointerfaces before hydration process. **h** SEM images of freeze-dried PEDOT:PSS hydrogels at the photocapacitor interface. Here the hydrogel that is optimized in Fig. 3 in terms of the charge injection amount with a ratio of 0.5 vol.% EG and 16 vol.% DMSO is provided.

RESULTS & DISCUSSION

Biointerface Device Structure

The biointerface architecture comprises an ITO conductive back electrode, zinc oxide (ZnO) electron transfer layer (ETL), poly(3-hexylthiophene) (P3HT) photoactive layer and conductive PEDOT:PSS hydrogel as the cell interfacial and hole transport layer (HTL) (Fig. 1a). The design facilitates superior charge extraction and injection performance,[33] in comparison with the designs only composed of the photoactive material and the conductive back electrode.[17,34] We chose indium tin oxide (ITO) on poly(terephthalate) (PET) as the transparent back electrode due to reduced faradaic effects. The ionic nature of the hydrogels supports the phase boundary between electronic and ionic charge carriers, connecting abiotic and biotic elements. Conductive PEDOT:PSS hydrogels were coated on P3HT layer by dry-annealing the modified aqueous PEDOT:PSS solution and then reswelling with deionized (DI) water or phosphate-buffered saline (PBS) (Fig. S1).[35] The compressive stress–strain curve shows an elastic linear region at strains smaller than 14% followed by a densification region. The nominal strain-stress curve (Fig. 1f) indicates that the average Young's modulus of 33-40 kPa is comparable to that of relevant tissues such as the brain (1-4 kPa) and cardiac tissue (10-18 kPa)[36] and orders of magnitude lower than rigid materials (MPa) used in conventional electrodes[27]. To confirm the presence of both PEDOT and PSS molecules, the X-ray photoelectron spectroscopy (XPS) spectral examination revealed the S 2P peaks at 168 eV and two peaks at 164 and 165 eV, which are

This article is protected by copyright. All rights reserved.

Accepted Article

related with the S atoms of PSS chains and S atoms of PEDOT chains, respectively (Fig. S2).[37] We also investigated the surface morphology of the biointerfaces before the PEDOT:PSS addition and after the dry-annealing process via atomic force microscopy (AFM) phase imaging, indicating increased surface roughness from 4.17 nm to 12.8 nm (Fig. 1g and Fig. S3). Moreover, biointerface interface had a 3D network with an average pore diameter of 55 μm (Fig. 1h). The increase in three-dimensional contact area due to the rough and porous nature of the PEDOT:PSS hydrogel potentially enlarge the capacitance on the surface and hence charge injection.[38]

Biointerface Operation and Optoelectronic Characterization

The biointerface operation starts with the exciton generation in the photoactive layer upon illumination. Due to the proper band alignment within the device, photo-generated electrons and holes dissociate toward opposite layers (Fig. 1d). As the lowest unoccupied molecular orbital (LUMO) energy level of ZnO, −4.6 eV, is lower than the LUMO level of P3HT, electrons are guided toward the back electrode and ZnO blocks the holes owing to its high bandgap energy. Likewise, the highest occupied molecular orbital (HOMO) energy level difference between P3HT and PEDOT:PSS accumulates the holes toward the hydrogel interfacial layer. While these materials were primarily chosen for the proper energy band alignment and superior performance, their biocompatibility was extensively studied and proven in the literature (ZnO,[39] P3HT,[14] PEDOT:PSS[40]). Additionally, as the HOMO energy of PEDOT:PSS is higher than the water oxidation energy, hole-based nonreversible faradaic reactions are highly limited.

The electrochemical activity of the PEDOT:PSS complex significantly depends on the hydrated pathways and the ion transport by PSS phase attractions.[41,42] However, this dependence induce

This article is protected by copyright. All rights reserved.

Accepted Article

conductivity problems for PEDOT:PSS polymeric films and stability problems for the hydrogels in aqueous medium.[35,41,42] Therefore, it is essential to engineer its composition co-solvent, dimethyl sulfoxide (DMSO),[35] and the conductivity enhancer, ethylene glycol (EG),[41] co-optimization while maximizing photocurrent and charge injection. To facilitate this, the photocurrent generation and amount of charge injection were investigated during the co-solvent, dimethyl sulfoxide (DMSO),[35] and the conductivity enhancer, ethylene glycol (EG),[41] co-optimization. The biointerfaces were immersed in modified artificial cerebrospinal fluid (aCSF) medium, as the electrolyte solution (Fig. 2a). To create the working condition in biological media, measurement system was operated with an amplifier ground immersed in the electrolyte without any wired ground connected to the device. The photocapacitor biointerfaces was excited with 445 nm, 50 $mW.cm^{-2}$, 5 Hz illumination (Fig. 2b). Photoelectrochemical current measurements revealed higher time constants and leading photocurrent peaks for the soft biointerface (Fig. 2c) that led to a 16-fold increase in total charge injection from 3.2 $\pm$ 0.3 pC to 51.1 $\pm$ 2.3 pC during charging phase with respect to the control device (ITO/ZnO/P3HT) (mean $\pm$ SEM, n = 12). As the ionic charge movement is the fundamental mechanism of the neural stimulation, the amount of charge in charging and discharging phases was evaluated by integrating the photocurrent transient[43] (Fig. 2d). The charge during the charging phase is balanced during the discharging phase showing the signature of safe capacitive current injection for neuron stimulation. We observed 0.5 vol.% EG and 16 vol.% DMSO facilitates the highest capacitive charge injection (Fig. 2e). Moreover, PBS is chosen as the water swelling medium for optimum hydrogel formation to increase electrochemical stability since it already contains the dominant ion species in extracellular fluid (ECF), such as H^+, K^+, Na^+ and Cl^-.[38,44] On the other hand, rehydration using deionized (DI) water also led to similar performance in terms of charge photogeneration. Furthermore, spatial confinement of photocurrent injection is crucial for the further studies with scaled-down biointerfaces. The photocurrent is spatially confined in the vicinity of the illuminated area (Fig 2f), which suggests the possible use of it for pixelated devices. As the geometrical interfacial surface area decreases,

This article is protected by copyright. All rights reserved.

Accepted Article

electrochemical impedance and consequently required threshold voltage increases[38], which can be potentially compensated with the volumetric capacitance of the hydrogels.[27]

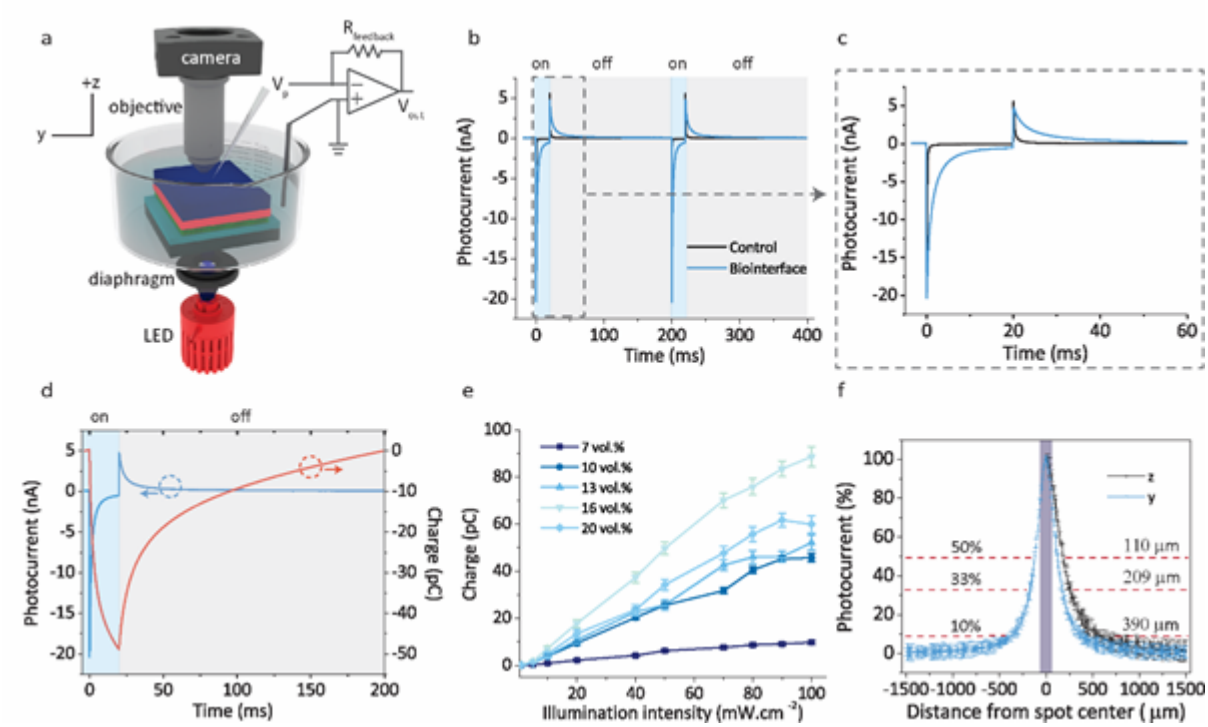


Fig. 2. a Schematic of the patch-clamp photocurrent measurements system. The glass pipette was positioned close to the surface and moved in +y and +z direction for spatial photocurrent characterization. **b** Photocurrent transient response upon excitation with trains of 20 ms, 50 mW.cm^{-2}, 5 Hz, 445 nm light pulses for control (black) and biointerfaces (blue). Blue and gray semi-transparent areas represent ON/OFF cycles of illumination, respectively. The gray dashed box represents the region of **c** close-up view to evaluate photocurrent rise and decay times. **d** Photocurrent transient (blue) for the optimized device with charge evaluation over one cycle of stimulus (red). **e** Charge injection amounts under different intensities for different DMSO concentrations in PEDOT:PSS hydrogels (mean ± SEM, n = 12). **f** Spatial current distribution by moving the patch pipette in +y and

This article is protected by copyright. All rights reserved.

Accepted Article

+z directions under illumination with 160 μm spot size. Photocurrent values at different positions were normalized with respect to the photocurrent peak at the center of the illumination spot.

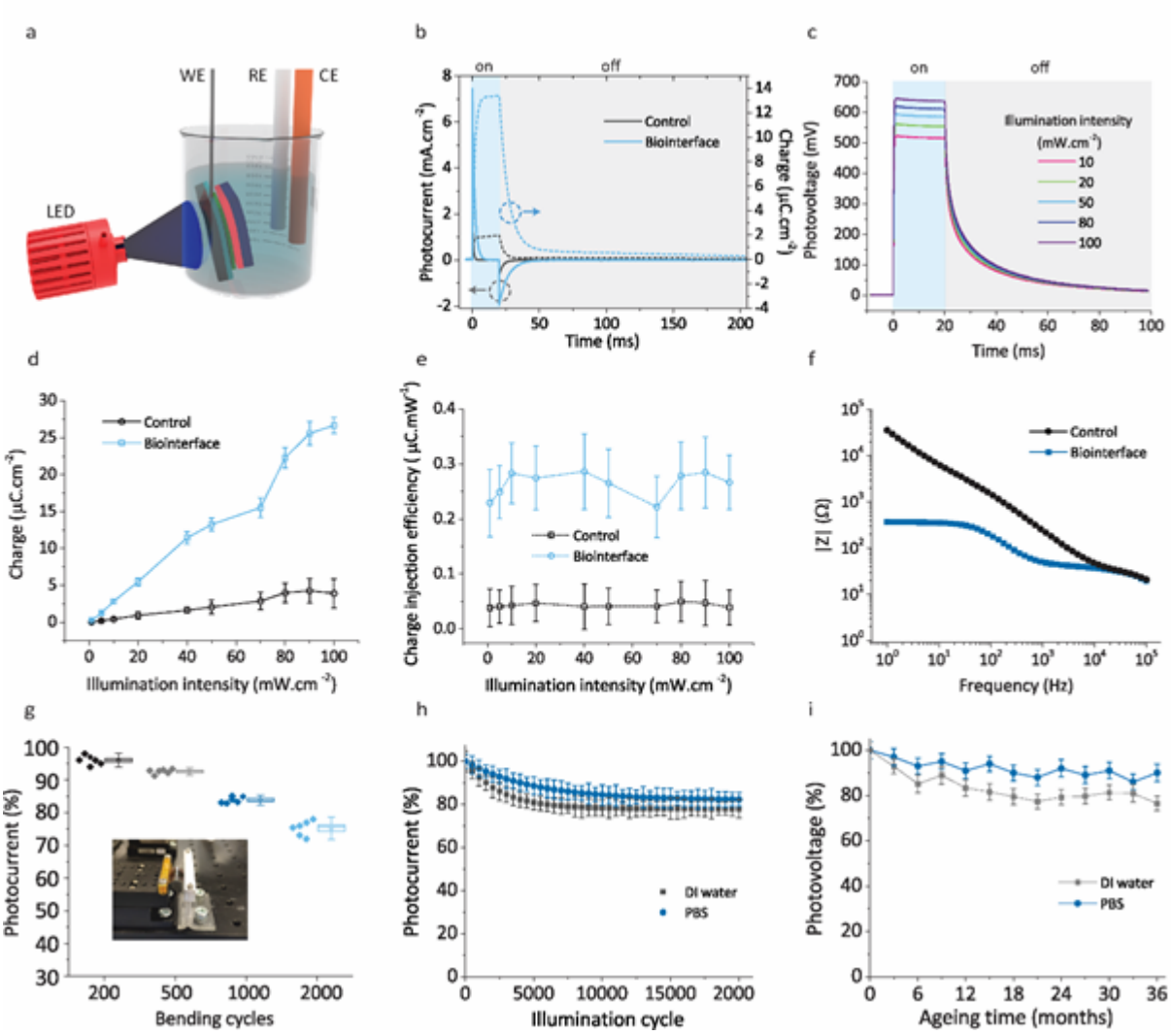
Photo-electrochemical characterization.

A three electrode electrochemical characterization is done to quantitatively analyze the ability of the optoelectrical signal transduction at the solid-liquid boundary (Fig. 3a).[38] Chronoamperometry measurements revealed biphasic charge-balanced transient during the turn-on and -off times of the illumination with suppressed faradaic contributions, which indicates the feature of a capacitive photoresponse (Fig. 3b). Consistent with the previous experiment using electrophysiology setup (Fig. 2e), 16 vol.% DMSO concentration generates the highest charge injection of 13.2 $\pm$ 1.4 μC.cm^{-2} under 50 mW.cm^{-2} (mean $\pm$ SEM, n = 20) (Fig. S4). The amount of charge injection satisfies the threshold charge density of ~10 μC.cm^{-2} for neural prostheses[45] and motivates its potential use for neural stimulation. The biointerfaces generate 601 $\pm$ 13 mV.cm^{-2} photovoltage (mean $\pm$ SEM, n = 20) under 50 mW.cm^{-2}, and more than 500 mV.cm^{-2} above 10 mW.cm^{-2} (Fig. 3c). Advantageously, biointerfaces can inject 4.6 $\pm$ 0.3 μC.cm^{-2} of charge at 20 Hz under 50 mW.cm^{-2} (mean $\pm$ SEM, n = 20) with fast rise time of ~61 μs, also indicating a capacitive behavior. Hydrogel photocapacitor provides an averaged ~7-fold higher charge injection performance over the control device (without hydrogel) under different illumination intensities (Fig. 3d). Furthermore, the amount of charge injection was normalized to the illumination intensity to evaluate charge injection efficiency (Fig. 3e) and ~6-fold improvement of charge injection efficiency is observed for biointerfaces with respect to the control. The electrochemical impedance spectroscopy revealed significant reduction in the electrochemical impedance for the biointerfaces and increase of the capacitance (Fig. 3f), which is favored for safe and efficient charge injection[45]. As the planar interfacial electrode area for control

This article is protected by copyright. All rights reserved.

Accepted Article

device and the biointerface kept constant, the reduced impedance for biointerfaces can be both attributed to the conductive electrode material, PEDOT:PSS, and also to the increased electrochemical surface area via hydrogel formation.[38] The responsivity corresponding to 156 mA/W and photovoltage levels (Fig. 3c) are higher than the other dry-material-based interfaces made of nanorod-carbon nanotube,[10] silicon dioxide,[46] metal and p-n semiconducting organic nanocrystals,[11] polymeric donor-acceptor and PEDOT:PSS based photovoltaic interfaces[13,15,16,47].



This article is protected by copyright. All rights reserved.

Accepted Article

Fig. 3. a Schematic of three-electrode potentiostat system. The biointerfaces were connected to the working electrode (WE) with a secondary counter electrode (CE) in a modified aCSF and the third electrode, reference electrode (RE), was introduced to obtain a reference potential independent of the current flow between WE and CE. The device area of 1 cm^2 was utilized to evaluate current and voltage generation. **b** Photocurrent transient for the biointerfaces (blue) and control (black) device (solid lines) with charge evaluation over one cycle of stimulus (dashed lines). **c** Photovoltage transient response for biointerfaces under different illumination intensities. **d** Charge injection and **e** charge injection efficiency for biointerfaces (blue) and control (black) devices under different illumination intensities. **f** Bode modulus of the control device (black) and biointerfaces (blue) in the frequency range of 1-10 kHz. **g** Normalized photocurrent performance for biointerfaces under 2000 cycles of bending. (inset: bending test setup) **h** Cyclic photostability experiment. PEDOT:PSS hydrogels were formed in either DI water (grey) or PBS (blue). Photocurrent peaks were measured over 20000 cycles and normalized to the value in the first cycle. **i** Photovoltage retention during reactive passive accelerated ageing test. Biointerfaces with PEDOT:PSS hydrogels formed in (DI) water or phosphate buffered saline (PBS) were placed in physiological saline solution at 87 °C. For **d**, **e**, **h**, **i** data represents mean ± SEM, n = 20 and for **g** mean ± SEM, n = 6.

Stability and Biocompatibility Tests

Instead of their rigid counterparts, next generation neural interfaces also require flexibility for conformal integration with the targeted tissues. While flexibility reduces mechanical mismatch between the biointerface and targeted tissue, maintaining optoelectronic performance against bending enables their long-term robustness after implantation. The biointerfaces are also flexible and they retained 75.2% of original photocurrent generation performance after 2000 bending cycles (Fig. 3g). Moreover, a capacitive electrode needs to sustain its capacitive charge injection over many cycles without increase in faradaic current. Hence, the enhanced charge injection due to PEDOT:PSS hydrogel formation on the surface is beneficial only if the capacitive charge injection is maintained

This article is protected by copyright. All rights reserved.

Accepted Article

over long periods. To evaluate this, cyclic stability test was carried out for 20000 stimulation cycles (Fig. 3h), and the photocurrent peak retention of 82.6 $\pm$ 4.9% was measured for the biointerfaces (mean $\pm$ SEM, n = 20). Although the photocurrent peak saturated around ~80% of its initial value, capacitive charge injection only reduced by 4.7 $\pm$ 0.7% while faradaic charge injection increased by 2.6 $\pm$ 0.4% of its initial value (mean $\pm$ SEM, n = 20). The similar charge balance between two phases of the photocurrent cycles indicated minimally faradaic mechanism dominated by the capacitive charge injection.[38] Moreover, the biointerface formed in PBS showed higher cyclic stability than the ones formed in DI water (Fig. 3h), supporting our claim that rehydration in PBS improves stability in modified aCSF.

To evaluate the device performance for extended periods, accelerated ageing tests provide insights for long-term use. For this purpose, elevated temperature of 87 °C was utilized to increase the kinetic energy of the system which escalate the rate of potential reactions. The aging factor is calculated as five times by the Arrhenius law, $acceleration\ factor\ (f) = 2^{\Delta t/10}$ where Δt = 87 °C – 37 °C assuming body temperature of 37 °C. The biointerfaces rehydrated in PBS were immersed in aCSF and kept at 87 °C to investigate photovoltage performance during accelerated ageing tests. The photovoltage was retained by 92 ± 2.8% after 4.5 weeks, corresponding to ~36 months of functional stability (Fig. S5). Moreover, 30 mM of H_2O_2 was added to the aCSF solution to account for the potential inflammatory response and to evaluate reactive accelerated aging (RAA).[48–50] Similar to the cyclic stability tests, hydrogels formed in PBS showed more robust performance in RAA tests, in comparison with the ones formed in DI water. The biointerface exhibited 91 $\pm$ 4.3% photovoltage retention after 4.5 weeks of RAA test, indicating functional stability over 3 years. (Fig. 3i) (mean $\pm$ SEM, n = 20). High performance retention in passive accelerated ageing test can be attributed to the ion rich hydrogel formation. Normally, hydrophilic polymers are sensitive to hydrolytic processes

This article is protected by copyright. All rights reserved.

Accepted Article

since water may penetrate easily into their internal structures.[38,51] As the PEDOT:PSS hydrogels were formed within PBS, the ion diffusion between highly ionic ECF and hydrogel is limited, which reduces the ionic exchange between two phases causing minimal performance loss for extended periods. The lower optoelectronic stability of hydrogels in DI water also supports this claim. Furthermore, to evaluate any redox reactions due to faradaic reactions, the biointerfaces were immersed in electrolytic solution and pH was monitored both under 45 minutes continuous and 5 Hz pulsed illumination. The minimal pH change of at most 0.03 strongly indicated that faradaic processes are highly unlikely under excitation of the biointerface (Fig. S6). Thus, the robustness of the biointerface were proven by the mechanical stress, cyclic stability, and reactive accelerated aging tests with high retention of optoelectronic performance.

We investigated the biocompatibility of the biointerface on primary hippocampal neurons and cardiac myocytes. Cell viability measurements using 3-(4,5- dimethylthiazol-2-yl)-2,5-diphenyl tetrazolium bromide (MTT)[52] indicated high cell viability in comparison with the glass/ITO control substrates for both primary hippocampal neurons and cardiac myocytes (Fig. 4a, b). The biointerfaces did not show any significant toxicity on both hippocampal neurons ($p = 0.3279$) and cardiac myocytes ($p = 0.1947$). Moreover, primary hippocampal neurons cultured on the biointerfaces did not show any negative morphological changes after 14 days under phase-contrast microscopy (Fig. S7) and immunofluorescence staining (Fig. 4c). Both presence of NeuN staining and morphological distribution of filamentous actin (F-actin) after 14 days indicated biocompatibility of the biointerfaces on neural cells. Likewise, Troponin T and F-Actin staining of cardiac myocytes showed that the biointerface has good biocompatibility with cardiac cells even after 14 days (Fig. 4d). The good biocompatibility exhibited by the biointerface is in good agreement with the previous studies

This article is protected by copyright. All rights reserved.

Accepted Article

examining each compound in our design separately.[16,53] Especially, hydrogel studies suggest that porous nature and microscale surface morphology supports the cell attachment.[27]

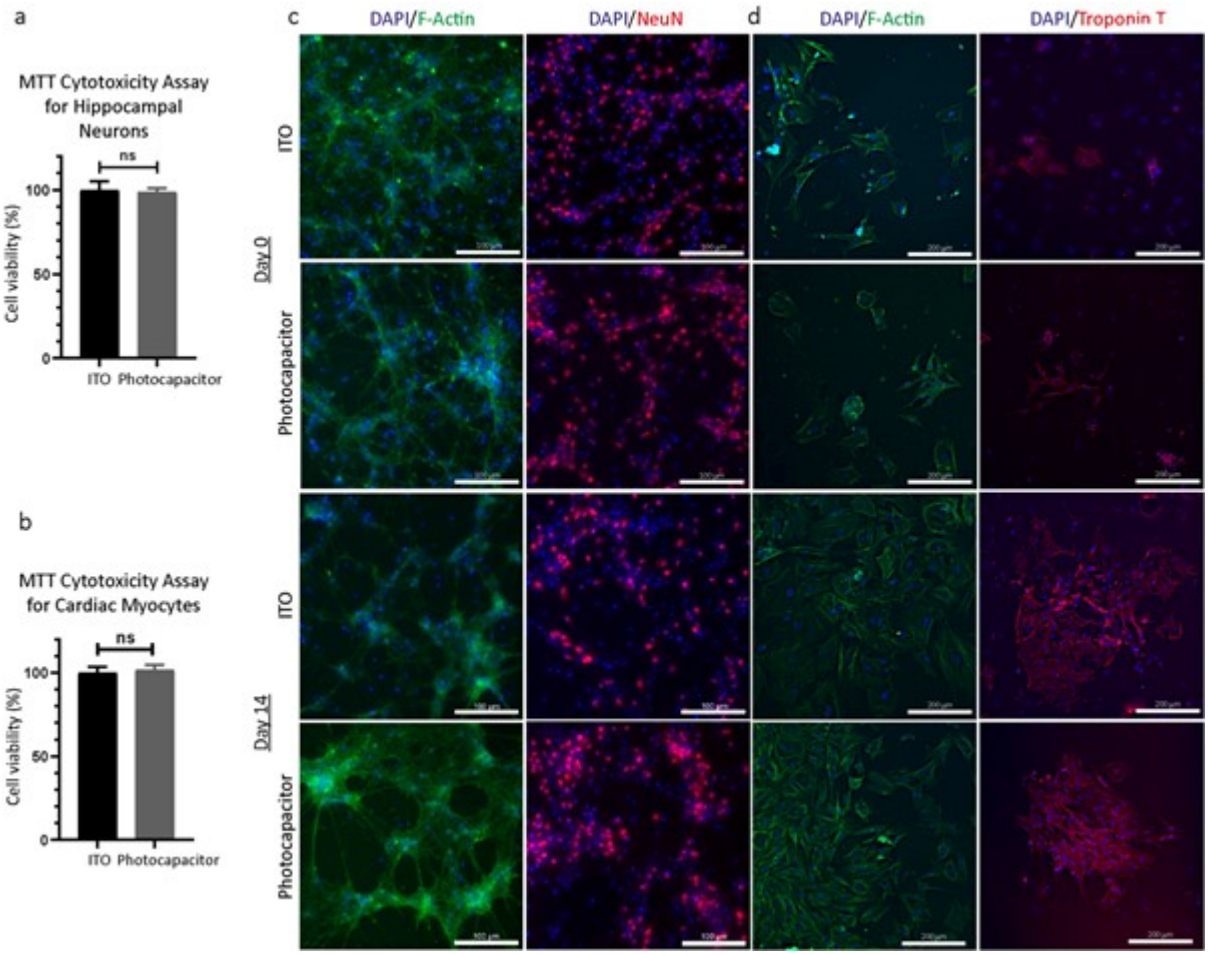


Fig. 4. The effect of the biointerface on metabolic activity of **a** primary hippocampal neurons and **b** primary cardiac myocytes was investigated by MTT viability assay in comparison with the ITO controls. An unpaired two-tailed t-test was performed to determine the level of significance. Each experiment was carried out with at least four biological replicates (mean ± SD, n = 4). *$p < 0.05$ was considered as statistically significant, and nonsignificant differences are presented as "ns". Immunofluorescence images of **c** primary hippocampal neurons and **d** cardiac myocytes on the

This article is protected by copyright. All rights reserved.

Accepted Article

biointerfaces and ITO controls at day 0 and day 14. Primary hippocampal co-stained with DAPI (blue), Anti-NeuN (red), and Anti-F-actin (green) (scale bar: 100 μm). Cardiac myocytes co-stained with DAPI (blue), Anti-F-actin (green), and Troponin T (red) (scale bar: 200 μm).

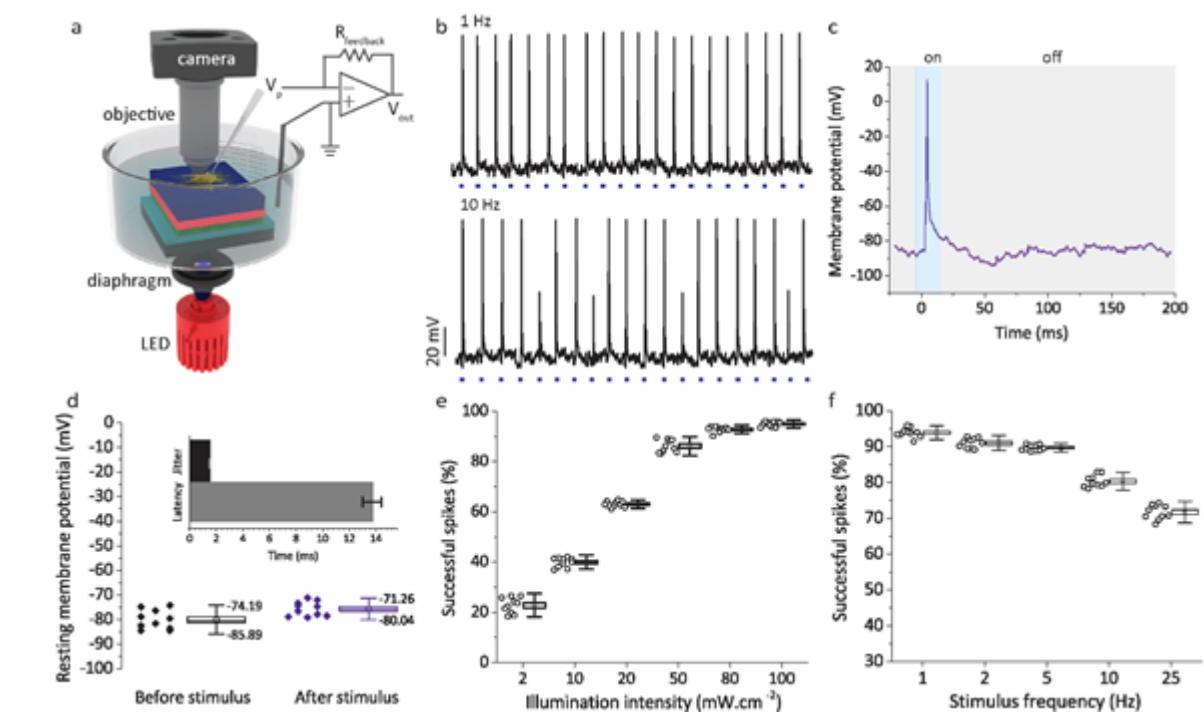
Photostimulation of hippocampal neurons.

Primary hippocampal neuron culture is one of best in vitro neuron models to examine the modulation of action potential activity.[54] Since the biointerface exhibited efficient optoelectronic transduction, high stability, and biocompatibility, we initially investigated light-triggered modulation of neural activity of primary hippocampal neurons that are cultured on the biointerface. The changes in intracellular membrane potential with respect to a distant Ag/AgCl reference electrode were measured using a patch-clamp system without any applied bias (Fig. 5a) and during all electrophysiology experiments, the I-V curve of the neurons was periodically measured to ensure the cell integrity. For example, trains of 20 ms pulses at 1 and 10 Hz were used for the optical excitation (Fig. 5b) and we observed above-threshold depolarizations leading the neural activation (Fig. 5c) with 90.1 $\pm$ 1.2% success ratio (mean $\pm$ SEM, n = 10). During the electrophysiology experiments, the resting membrane potential before and after 1 min, 5 Hz optical stimulation was measured to observe any significant adverse effect on electrophysiology experiments (Fig. 5d). Owing to capacitive nature of the stimulation, resting membrane potentials did not show any significant difference between ITO control device and biointerface (before optical stimulation, Student's t-test, P = 0.0973, n = 10; after optical stimulation, Student's t-test, P = 0.1363, n = 10). The calculated mean ($\pm$ s.e.m) latency of 13.9 $\pm$ 0.4 ms and the jitter (standard deviation of latencies for all measured neurons) of 1.8 $\pm$ 0.11 ms indicates short latency and jitter for the stimulation with the biointerface (Fig. 5e).[55] To evaluate the effect of illumination intensity, the same excitation pulses were utilized with different intensities ranging from 2 to 100 mW.cm^{-2}. Our device can elicit action potentials even under low light

This article is protected by copyright. All rights reserved.

Accepted Article

intensities as low as 20 mW.cm^{-2} (Fig. 5e). Likewise, neural activity in response to different excitation frequencies indicated more than 70% successful activation ratio at 25 Hz stimulation (Fig. 5f). To investigate the photothermal and thermocapacitive effects, maximum temperature induction due to optical excitation was calculated (Supplementary Note 1). Even under the highest intensity, 100 mW.cm^{-2} used in this study, the temperature changes of 0.364 °C is not sufficient to elicit photothermal stimulation of neurons.[34] Supporting this claim, recorded neural response under continuous light excitation did not indicate any depolarization or hyperpolarization. Moreover, if the biointerface would be utilized as a retinal prosthesis, light intensity threshold of 20 mW.cm^{-2} for neural stimulation is lower than the maximum permissible chronic radiant exposure for ocular safety (54 mW.cm^{-2}).[24,56]



This article is protected by copyright. All rights reserved.

Accepted Article

Fig. 5. a Schematic of electrophysiology patch-clamp measurement system. **b** Neural activity of primary hippocampal neurons cultured on the biointerfaces excited with a train of 10 pulses (20 ms, 50 mW.cm^{-2}, 1 and 10 Hz). **c** Representative single action potential during on and off cycles. **d** The resting membrane potential of neurons cultured on the biointerfaces before (black) and after (purple) 1 min optical excitation at 5 Hz (mean ± SEM, n = 10). Inset: The mean latency of the action potential peak and the jitter as the standard deviation of latencies of all measured neurons (mean ± SEM, n = 10). Successful spike ratio **e** under different illumination powers and **f** at different frequencies (mean ± SEM, n = 10).

Photocontrol of cardiac myocytes.

We further investigated the optical control of beating frequencies of cardiac myocytes cultured on the biointerface. By using patch-clamp measurements we initially observed beating pattern of cardiac myocytes with frequencies ranging from 400 to 900 mHz (Fig. 6a). After starting optical excitation, we observed fast and reversible changes in spontaneous beating frequency of cardiac myocytes. For example, the representative intracellular recording of cardiac myocytes stimulated with 5 pulses at 4 Hz also shows the capacitive stimulation (Fig. 6b). For modulation of the beating frequency, while under 1 Hz optical excitation the beating frequency increased to 820 mHz, by tuning the optical excitation to 5 Hz the beating frequency further increased to 2900 mHz. Since we did not observe accumulation of photogenerated charge carriers after discharging phase (Fig. 2d), reversible steady-state depolarizations were expected. To support our claim, we conduct intracellular recordings of cardiac myocytes before, during and after the stimulation. The steady state beating frequency of ~650 mHz retained after the stimulation with 20 pulses indicating capacitive stimulation (Fig. 6a). Moreover, these results are consistent with the photocurrent measurements and electrophysiology experiments on primary hippocampal neurons that returned to their resting membrane potentials after

This article is protected by copyright. All rights reserved.

Accepted Article

stimulation (Fig. 5d). Furthermore, we investigated photostimulation success rate of cardiac myocytes at different excitation intensity ranging from 10 to 250 $mW.cm^{-2}$. Above 150 $mW.cm^{-2}$ we observed successful beating of cardiac myocytes above 93% success rate (Fig. 6c). While we decrease the light intensity level, we started to observe the decrease of the beating success and reached to 60% at the light intensity level of 80 $mW.cm^{-2}$ (Fig. 6c). Moreover, we conduct stimulus frequency dependent experiments and starting from 0.5 Hz to 10 Hz, biointerfaces elicit cardiac action potentials with ~95% success rate and even has potential to achieve >80% at 5 Hz (Fig. 6d). The decrease in the stimulation success for higher frequencies can be attributed to the cardiac refractory period. Finally, to explore the activation of Ca^{2+} channels in stimulated cardiac myocytes, they were treated with a common voltage gated Ca^{2+} channel blocker (Cd^{2+}). We measured cardiac myocyte membrane potential with intracellular Cd^{2+} (30, 50 and 100 μM for inhibitory but nontoxic concentrations)[57] treatment, which reduces the cardiac action potential duration. In phase 2 of cardiac action potential, influx of Ca^{+2} electrically balances the K^+ efflux through delayed rectifier K^+ channels. Increasing concentrations of Cd^{+2} reduces the plateau during phase 2 and action potential duration as expected (Fig. 6e).

This article is protected by copyright. All rights reserved.

Accepted Article

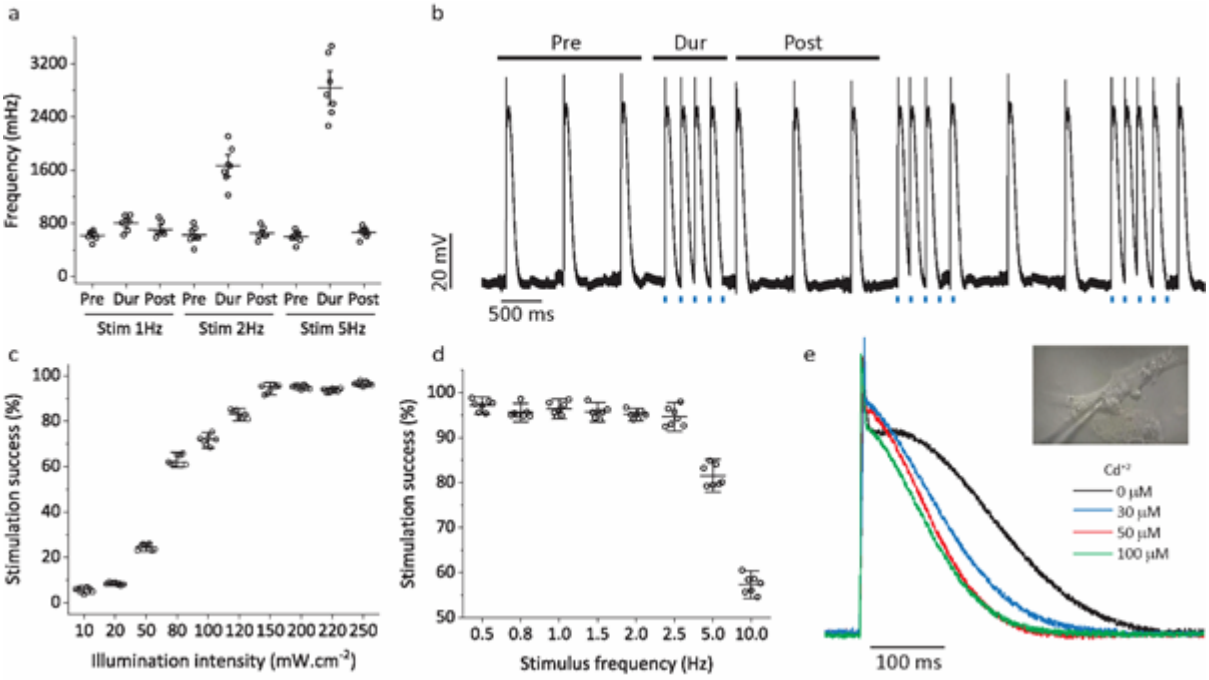


Fig. 6. a Cardiac myocyte response for stimulation frequencies of 1, 2 and 5 Hz. The cellular activity was monitored using a patch-clamp electrophysiology system. The cardiac action potential frequency for seven data points (i.e. recorded from 7 cells) for prestimulation (pre), during stimulation (dur) and poststimulation (post) condition are plotted with mean ± SEM. For this stimulation experiments, cardiac myocyte activity was measured for 2 min prestimulation before 20 light pulses with different frequencies were applied. Beating frequency at poststimulation condition was measured for 2 min after stimulation. **b** Patch-clamp electrophysiology recordings for a representative cell, from a group of 7 cardiac myocytes that were stimulated with 5 pulses of 445 nm, 200 $mW.cm^{-2}$. **c** Stimulation success under different illumination intensities and **d** at different stimulation frequencies was calculated. The same measurement conditions with **a** applied to 7 cardiac myocytes. The data is represented as mean ± SEM, n = 7. **e** Representative membrane potential transients of 30, 50 and 100 µM Cd^{2+}-treated and non-treated individual cardiac myocytes (inset: image of a patch-clamped cardiac myocyte).

DISCUSSION

This article is protected by copyright. All rights reserved.

Accepted Article

Since the conventional electrodes are limited in terms of their distinct properties from the cell/tissue environment as being dry and solid, today there is a growing interest on hydrogel bioelectronics.[27] Hydrogels provide a promising material platform bridging biology and electronics with matching mechanical and structural properties. So far, PEG hydrogels were advantageously used as a cell-encapsulating waveguide for light-based communication with optogenetically-modified cells for sensing and therapy,[31,58] and silk protein hydrogels was also utilized as a biomolecule- and light-transmissive biomaterial incorporating melanin nanoparticles for light-meter sensor.[32] In this study, we demonstrated that the hydrogels exhibit high potential for optoelectronic biointerfaces for efficient and safe optical stimulation of neurons and cardiac myocytes.

We showed that the hydrogel-enabled biointerface can facilitate action potential generation in neurons and cardiac myocytes below 50 $mW.cm^{-2}$ and 150 $mW.cm^{-2}$, respectively, which is the most efficient flexible optoelectronic biointerface beside its tissue/cell bridging properties. Moreover, the charge levels that can be produced by this biointerfaces is also within the range for in-vivo retinal implants with responsivity of 156 mA/W that can be potentially used against the retinal degeneration diseases such as age-macular degeneration and retinitis pigmentosa.

Optical control of the cardiac myocytes by flexible, efficient and hydrogel-based biointerfaces also has high potential toward wireless optoelectronic pacemaker implants. Cardiac problems are the leading cause of deaths[59] and for the various cardiac rhythm disorders cardiac pacemakers are effective treatment option. But conventional cardiac pacemaker systems are bulky and wired, and light-triggered control of cardiac rhythm during fibrillation and arrhythmia conditions can enable a less-invasive treatment for these life-threatening situations. There were some recent progresses on that

This article is protected by copyright. All rights reserved.

Accepted Article

goal using different material systems by using silicon nanowires[8] and graphene[9]. For example, laterally-embedded silicon-nanowires in an polymer were realized, but they control the neural activity via photo-electrochemical faradaic currents that are suggested to be suppressed for long-term neural implants.[8] Moreover, Si nanowires grown directly on aluminum thin foils[60] and graphene[9] were also investigated, even though the capacitive stimulation is hypothesized, it is not quantitatively shown. Particularly, the proposed capacitive stimulation of cardiac myocytes is fundamentally different than the previous optical methods that depend on faradaic reactions, heating, and optogenetics.[61–65] Besides, these implants can be also integrated for conformal contacts with cerebral cortex and vagal nerve stimulation as well.[7,66] Hence, these flexible, efficient and robust biointerfaces show high promise.

Toward a more viable solution for implants, there are several challenges in this study that need to be addressed. The first one is currently that the wavelength of the communication in this study is within the visible range. For future retinal and cardiac implants, the operational wavelength needs to be shifted toward near-IR. By this way, for the patients having age macular degeneration, the remaining healthy photoreceptors will not be activated while the degenerated retinal parts will be stimulated.[67] For retinal applications, since the hydrogel is not transparent, a subretinal implantation is not possible. Hence, with the near-IR extension, such a device can be used with epiretinal implantation. For subretinal implantation, alternative transparent hydrogels need to be investigated. For cardiac application, light-penetration into deep-tissue is required, which can be solved by biopolymer waveguides and fibers.[68] Alternatively, near-IR photoresponse will facilitate light penetration into deep-tissue for energizing the implant with an external or sub-cutaneous implanted light source. To reduce the electrode size, advanced fabrication techniques such as 3D printing and ink-jet printing

This article is protected by copyright. All rights reserved.

Accepted Article

have been utilized for conductive hydrogels.[27,69,70] Moreover, PEDOT:PSS hydrogels can be also patterned with high resolution using the electrochemical gelation method.[71]

CONCLUSION

In summary, in this study we demonstrated that hydrogels significantly enhance the safe capacitive charge injection efficiency of optoelectronic biointerfaces with negligible faradaic processes while facilitating tissue-like biomechanical properties. The flexible biointerface retained their optoelectronic performance under mechanical, optical, and electrochemical stress, and exhibited high biocompatibility owing to their porous, soft, and ion-rich interfacial nature. The biointerface enabled light-triggered stimulation and control of neurons. Therefore, we anticipate that hydrogel based wireless optoelectronic biointerfaces show great promise for developing truly noninvasive, versatile, and safe implants for future photomedicine.

MATERIALS & METHODS

Biointerface Fabrication. The devices were fabricated onto the ITO coated PET substrates for optoelectronic performance optimization, (Sigma-Aldrich, 639303). The PET/ITO substrates were cleaned by sonication in sodium hydroxide (NaOH) solution for 5 min, then immersed in tension-active agent:deionized water (HELLMANEX III, 3%) for 15 min. The substrates were washed out with deionized water then sonicated for 15 min, in absolute ethanol for 5 min and at the end, in isopropyl alcohol (IPA) for 5 min all at 50°C. The cleaned substrates were placed in UV-ozone cleaner for 25 min. For ZnO coating, ZnO precursor composed of 109 mg zinc acetate dehydrate ($Zn(CH_3CO_2)_2 \cdot 2H_2O$), Sigma-Aldrich, in 1 ml of 2-methoxyethanol ($C_3H_8O_2$) and 40 mg of ethanolamine ($HOCH_2CH_2NH_2$) placed in sonication bath for 30 min at 50 °C. Then, the ZnO precursor solution was filtered by a 0.45 μm PVDF filter. The precursor solution was spin coated onto

This article is protected by copyright. All rights reserved.

Accepted Article

the PET/ITO substrates at 2000 rpm for 60 s, and annealed at 150 °C for 45 min. The consecutive layer, P3HT (95.7% regioregular) (>99% pure, Ossilla) was prepared as 25 mg ml^{-1} solution of P3HT in o-dichlorobenzene, and stirred for overnight at 70°C. P3HT layer was fabricated onto ZnO layer by spin coating at 1000 rpm for 150 s and annealed at 150°C for 15 min. For the PEDOT:PSS hydrogel formation different DMSO (7, 10, 13, 16, 20 vol.%) and EG (0, 0.5, 1, 2 vol.%) concentrations were utilized for improving hydrogel formation and optoelectronic performance. PEDOT:PSS solution mixed with DMSO and EG was stirred for overnight at room temperature. Then, the solution was drop-casted onto PET/ITO/ZnO/P3HT device and annealed for 3 hours at 40°C. A disc shaped sample of 8 mm diameter and 2 mm height was cut from the original sample. Compression test was carried out using Anton-Paar rheometer (MCR-302) in compression mode with a rate of 1 mm/min at 25°C**.** The surface morphology of the dried PEDOT:PSS layers was measured using AFM (Bruker Instruments). For the cross-sectional SEM (Zeiss ultra plus field emission SEM) images, PEDOT:PSS hydrogels were immersed in liquid nitrogen before the measurement.

Photocurrent Measurements. The optoelectronic characterizations were carried out by Olympus T2 upright microscope and extracellular patch clamp (EPC 800 patch clamp amplifier, HEKA Elektronik GmbH, Pfalz, Germany). The modified aCSF solution was prepared by mixing 10 mM of 4-(2-hydroxyethyl)-1- piperazineethanesulfonic acid (HEPES), 10 mM of glucose, 2 mM $CaCl_2$, 140 mM of NaCl, 1 mM of $MgCl_2$, 3 mM of KC and mixed with the distilled water. The pH was calibrated to 7.4 using 1M NaOH. Thorlabs' blue (M450LP1) and the LED driver DC2200 (Thorlabs Inc, NJ, USA) were used for excitation. Measurements were obtained without grounding the bottom ITO layer, and the ground was immersed into the aCSF solution.

Photo-electrochemical Measurements. For the chronoamperometry, chronopotentiometry and electrochemical impedance characterization, an Autolab system (Potentiostat Galvanostat PGSTAT, Metrhom, Netherlands) was utilized. The three-electrode electrochemical measurement system consists of Ag/AgCl as the reference electrode, platinum wire as the counter electrode and connection to the ITO layer of the biointerfaces as the working electrode, all immersed in modified aCSF medium. The control device and biointerfaces were excited with the same excitation system with the optical power meter, Newport 843-R. The data was analyzed using the NOVA software.

pH Monitoring

This article is protected by copyright. All rights reserved.

Accepted Article

PEDOT:PSS hydrogel coated photocapacitor biointerfaces were placed in galvanostat measurement chambers (Metrhom, Netherlands) and filled with 50 ml of electrolytic solution of 3.0 mM $CaCl_2$, 1.5 mM $MgCl_2$, 124 mM NaCl, 3.0 mM KCl, 26mM $NaHCO_3$, and 1.0 mM NaH_2PO_4. Under 45-min illumination with 445 nm, 100 $mW.cm^{-2}$ light, pH measurements were carried out in every 5 min using Mettler Toledo.

Ethical Usage of Animals. All experimental procedures involve on animals carried out by responsible veterinarian and certified researchers for animal experiments. The study approved by the Ethical Experimental Animal Usage Committee of Koç University (Approval No: 2019.HADYEK.023) according to European Parliament's Directive 2010/63/EU on Protection of Animals Used for Scientific Purposes.

Primary Hippocampal Neuron Isolation and Culture. Primary hippocampal neuron isolation and culture protocol made as described in our previous studies.[24,72] In brief, pregnant rat between embryonic day 15 to day 17 euthanized and hippocampal regions of embryos extracted. The hippocampi of embryos trypsinized in 0.25% Trypsin-EDTA solution (Thermo Fisher Scientific, MA, USA) with 2% DNase-I supplement (NeoFroxx, Einhausen, Germany), triturated, and centrifuged for dissociation of the neural tissue. Dissociated neural tissue mixed with Neurobasal Medium (NBM, Thermo Fisher Scientific, MA, USA) supplemented with B27, L-glutamine, β-mercaptoethanol, glutamate (Thermo Fisher Scientific, MA, USA) and passed through a 70 µm cell strainer. Then the cell suspension seeded on poly-L-lysine (PLL, Sigma-Aldrich, MO, USA) coated biointerfaces and ITO substrates. After 3-days incubation, the cell media changed with NBM supplemented with cytosine arabinoside (Sigma-Aldrich, MO, USA) to inhibit glia growth. After 24-hour incubation with cytosine arabinoside, primary hippocampal neural cells on the substrates maintained in NBM at 37 °C in a cell incubator until used for the further experiments.

Primary Cardiac Myocyte Isolation and Culture. After euthanasia, the hearts of the E15-E17 Wistar Albino rats removed by cutting sternum. The hearts were washed with DMEM/F12 without any supplement and were divided to the four pieces. The cardiac muscles were incubated in 0.25% Trypsin-EDTA solution (Thermo Fisher Scientific, MA, USA) with 0.1% Collagenase (Type I, Sigma Aldrich, MO, USA), 5 mM $CaCl_2$ (Sigma Aldrich, MO, USA), and (2% DNase-I supplement (NeoFroxx, Einhausen, Germany) for 20 minutes in a 37 °C incubator with an orbital shaker. Then DMEM/F12 with 10% FBS added to inhibit digestion and the cells were centrifuged. After the centrifuge, the supernatant was changed with complete DMEM/F12 supplemented with cytosine

This article is protected by copyright. All rights reserved.

Accepted Article

arabinoside (Sigma-Aldrich, MO, USA) to inhibit growth of the non-muscle cells. Then cells were triturated until all the tissue dissolved in the medium. The cells were seeded on a non-coated T-75 flask and incubated at 37 °C in a 5% CO_2, 85% humidified incubator for an hour. After non-muscle cells were attached to the non-coated T-75 flask, the supernatant taken, and the number of the cells in the medium counted. Then the cardiac muscle cells were seeded on the collagen coated biointerfaces and ITO substrates. The cardiac myocytes on the substrates were kept at 37 °C in a 5% CO_2, 85% humidified incubator for two days and the myocytes were maintained in complete DMEM/F12 until the experiments. To prevent calcium paradox related cell damage on cardiac muscle cells, total calcium concentration range in all cell media (2-5 mmol) kept in the same levels during all experimental procedures.

In vitro Biocompatibility Assay. Cell viability of primary hippocampal neurons on the substrates analyzed with MTT cytotoxicity assay, which is described in detail in our previous study.[15] Briefly, the substrates were sterilized with 70% ethanol and 30 minutes UV irradiation and placed in 6-well plates. The primary hippocampal neurons and cardiac myocytes were isolated and cultured (5×10^5 cells per sample) on the substrates in a humidified incubator at 37 °C with 5% CO_2. After 48-hours incubation, the cell media replaced with 1 ml of 5 mg/ml MTT solution (Thermo Fisher Scientific, MA, USA) and 4 ml NBM mixture per well and cells incubated at 37 °C for 4 hours. After 4 hours incubation samples transferred to new 6-well plate and 1:1 mixture of DMSO and ethanol added on wells to dissolve the formazan crystals. After 10 minutes dissolution period, the solution was transferred to a 96-well plate and the absorbance was measured at 600 nm and 690 nm wavelengths with Synergy-H1 Microplate Reader (Bio-Tek Instruments, VT, USA). The cell viability calculated as follows: cell viability percentage = $(OD_{sample}/OD_{control}) \times 100$.

Immunofluorescence Staining and Imaging. Immunofluorescence staining and imaging protocols made in a similar way of our previous article.[72] In short, primary hippocampal neurons ($2x10^5$ cells per sample) and primary cardiac myocytes ($1x10^5$ cells per sample) cultured as explained above and incubated for 24 hours on ITO substrates and the bio-interfaces at 37 °C in cell culture incubator. Then, samples fixated at same day (Day 0) or maintained in appropriate cell culture conditions for two weeks (Day 14). After incubation periods, the cells were fixated with 4% paraformaldehyde and washed three times with PBS-T (Phosphate Buffered Saline with 0.1% Triton X-100) before blocking with Superblock solution (Thermo Fisher Scientific, MA, USA). After blocking, the samples with primary hippocampal neurons were incubated with rabbit anti-NeuN antibody (ab177487, Abcam,

This article is protected by copyright. All rights reserved.

Accepted Article

Cambridge, UK) overnight at 4 °C and washed three times with PBS-T. Then, they were incubated with goat anti-rabbit IgG Alexa Fluor 555 (4413, Cell Signaling Technology, MA, USA) for fluorophore staining of anti-NeuN primary antibody for 90 minutes at 37 °C. In the meanwhile, the cardiac myocytes were also incubated with mouse anti-cardiac Troponin-T antibody (MA5-12960, Thermo Fisher Scientific, MA, USA) and the respective anti-mouse IgG Alexa Fluor 555 secondary fluorophore antibody (A28180, Thermo Fisher Scientific, MA, USA) in a similar way to primary neurons. Also, both cardiac myocytes and primary neurons were incubated with FITC-conjugated phalloidin antibody (P5282, Sigma-Aldrich, MO, USA) for 90 minutes at 37 °C for visualization of the cytoskeletons. For mounting samples, all samples were washed three times with PBS-T, then incubated in DAPI supplemented mounting medium (ab104139, Abcam, Cambridge, UK) to observe nuclei and sealed with nail polish on slides. Finally, immunofluorescence imaging was done by using an inverted immunofluorescence microscope (Axio Observer Z1, ZEISS, Oberkochen, Germany).

Electrophysiology Experiments. All electrophysiology experiments were carried out by EPC 800 patch clamp amplifier (HEKA Elektronik GmbH, Pfalz, Germany). The biointerfaces were cleaned with 70 vol% ethanol and incubated at 37°C for 3 days in deionized water. For the preparation of extracellular and intracellular medium solutions, and the use of LED excitation system, the same procedures in our previous reports were followed.[15,24] The pulled patch pipettes of 8-12 MΩ and 3-6 MΩ were utilized to carry out the whole-cell patch clamp experiment on primary hippocampal neurons and cardiac myocytes, respectively.

Data availability

The datasets that support all the findings of this study are available from the corresponding authors upon reasonable request.

Acknowledgement

This project has received funding from the European Research Council (ERC) under the European Union's Horizon 2020 Research and Innovation Programme (grant agreement no. 639846). S.N. also acknowledges the support by the Turkish Academy of Sciences (TÜBA-GEBIP; The Young Scientist Award Program); the Science Academy of Turkey (BAGEP; The Young Scientist Award Program); and Bilim Kahramanları Derneği (The Young Scientist Award Program). The authors gratefully acknowledge use of the services and facilities of the Koç University Research Center for Translational

This article is protected by copyright. All rights reserved.

Accepted Article

Medicine (KUTTAM), funded by the Republic of Turkey Ministry of Development. The content is solely the responsibility of the authors and does not necessarily represent the official views of the Ministry of Development. The authors thank Levent Beker and Berkay Kullukcu for the mechanical stress test. The authors thank Baris Yagci and Amir Motallebzadeh for SEM and AFM images at KUYTAM (Koc University Surface Science and Technology Center). The authors thank Prof. Burak Ülgüt at Bilkent University for his discussions on electrochemistry.

Author Contributions

M.H. planned experiments, fabricated photocapacitor biointerfaces, performed photostimulation, photo-electrochemical and electrophysiological experiments, analyzed the data and wrote the manuscript. E.Y. prepared primary hippocampal neuron and primary cardiac myocyte cultures, performed cell viability assays, immunofluorescence staining experiments, analyzed data and wrote the manuscript. H.N.K assisted to primary hippocampal neuron and primary cardiac myocyte cultures and cell viability assays. S.K. conducted mechanical characterization and interpreted the data. G.O.E. conducted XPS analysis and interpreted the data. I.B.D-Y built the optical setup for monitoring hydrogel formation and did the characterization. E.S. supervised the mechanical characterization and interpreted the data. A.S. interpreted and discussed the data and supervised primary hippocampal neuron culture, cell viability assays and fluorescence microscopy experiments. S.N. planned and supervised the entire study and wrote the manuscript. All the authors read and accepted the manuscript.

Competing Interests

The authors declare no competing interests.

Additional information

Supplementary information is available for this paper.

This article is protected by copyright. All rights reserved.

Accepted Article

REFERENCES

[1] A. M. Lozano, N. Lipsman, H. Bergman, P. Brown, S. Chabardes, J. W. Chang, K. Matthews, C. C. McIntyre, T. E. Schlaepfer, M. Schulder, Y. Temel, J. Volkmann, J. K. Krauss, *Nat. Rev. Neurol.* **2019**, *15*, 148.

[2] M. Chernov, A. W. Roe, *Neurophotonics* **2014**, *1*, 011011.

[3] K. Deisseroth, *Nat. Neurosci.* **2015**, *18*, 1213.

[4] P. Fattahi, G. Yang, G. Kim, M. R. Abidian, *Adv. Mater.* **2014**, *26*, 1846.

[5] T. Il Kim, J. G. McCall, Y. H. Jung, X. Huang, E. R. Siuda, Y. Li, J. Song, Y. M. Song, H. A. Pao, R. H. Kim, C. Lu, S. D. Lee, I. S. Song, G. Shin, R. Al-Hasani, S. Kim, M. P. Tan, Y. Huang, F. G. Omenetto, J. A. Rogers, M. R. Bruchas, *Science (80-.).* **2013**, *340*, 211.

[6] K. Mathieson, J. Loudin, G. Goetz, P. Huie, L. Wang, T. I. Kamins, L. Galambos, R. Smith, J. S. Harris, A. Sher, D. Palanker, *Nat. Photonics* **2012**, *6*, 391.

[7] Y. Jiang, X. Li, B. Liu, J. Yi, Y. Fang, F. Shi, X. Gao, E. Sudzilovsky, R. Parameswaran, K. Koehler, V. Nair, J. Yue, K. H. Guo, Y. Fang, H. M. Tsai, G. Freyermuth, R. C. S. Wong, C. M. Kao, C. T. Chen, A. W. Nicholls, X. Wu, G. M. G. Shepherd, B. Tian, *Nat. Biomed. Eng.* **2018**, *2*, 508.

[8] R. Parameswaran, K. Koehler, M. Y. Rotenberg, M. J. Burke, J. Kim, K. Y. Jeong, B. Hissa, M. D. Paul, K. Moreno, N. Sarma, T. Hayes, E. Sudzilovsky, H. G. Park, B. Tian, *Proc. Natl. Acad. Sci. U. S. A.* **2019**, *116*, 413.

[9] A. Savchenko, V. Cherkas, C. Liu, G. B. Braun, A. Kleschevnikov, Y. I. Miller, E. Molokanova, *Sci. Adv.* **2018**, *4*, eaat0351.

[10] L. Bareket, N. Waiskopf, D. Rand, G. Lubin, M. David-Pur, J. Ben-Dov, S. Roy, C. Eleftheriou, E. Sernagor, O. Cheshnovsky, U. Banin, Y. Hanein, *Nano Lett.* **2014**, *14*, 6685.

[11] D. Rand, M. Jakešová, G. Lubin, I. Vėbraitė, M. David-Pur, V. Đerek, T. Cramer, N. S. Sariciftci, Y. Hanein, E. D. Głowacki, *Adv. Mater.* **2018**, *30*, 1707292.

[12] D. Ghezzi, M. R. Antognazza, M. Dal Maschio, E. Lanzarini, F. Benfenati, G. Lanzani, *Nat. Commun.* **2011**, *2*, 166.

[13] N. A. L. Chenais, M. J. I. Airaghi Leccardi, D. Ghezzi, *Commun. Mater.* **2021**, *2*, 28.

[14] D. Ghezzi, M. R. Antognazza, R. MacCarone, S. Bellani, E. Lanzarini, N. Martino, M. Mete, G. Pertile, S. Bisti, G. Lanzani, F. Benfenati, *Nat. Photonics* **2013**, *7*, 400.

[15] M. Han, S. B. Srivastava, E. Yildiz, R. Melikov, S. Surme, I. B. Dogru-Yuksel, I. H. Kavakli, A. Sahin, S. Nizamoglu, *ACS Appl. Mater. Interfaces* **2020**, *12*, 42997.

This article is protected by copyright. All rights reserved.

Accepted Article

[16] S. B. Srivastava, R. Melikov, E. Yildiz, M. Han, A. Sahin, S. Nizamoglu, *Biomed. Opt. Express* **2020**, *11*, 5237.

[17] J. F. Maya-Vetencourt, D. Ghezzi, M. R. Antognazza, E. Colombo, M. Mete, P. Feyen, A. Desii, A. Buschiazzo, M. Di Paolo, S. Di Marco, F. Ticconi, L. Emionite, D. Shmal, C. Marini, I. Donelli, G. Freddi, R. MacCarone, S. Bisti, G. Sambuceti, G. Pertile, G. Lanzani, F. Benfenati, *Nat. Mater.* **2017**, *16*, 681.

[18] D. I. Medagoda, D. Ghezzi, *Commun. Mater.* **2021**, *2*, 111.

[19] J. F. Maya-Vetencourt, G. Manfredi, M. Mete, E. Colombo, M. Bramini, S. Di Marco, D. Shmal, G. Mantero, M. Dipalo, A. Rocchi, M. L. DiFrancesco, E. D. Papaleo, A. Russo, J. Barsotti, C. Eleftheriou, F. Di Maria, V. Cossu, F. Piazza, L. Emionite, F. Ticconi, C. Marini, G. Sambuceti, G. Pertile, G. Lanzani, F. Benfenati, *Nat. Nanotechnol.* **2020**, *15*, 698.

[20] A. Qu, M. Sun, J. Y. Kim, L. Xu, C. Hao, W. Ma, X. Wu, X. Liu, H. Kuang, N. A. Kotov, C. Xu, *Nat. Biomed. Eng.* **2021**, *5*, 103.

[21] T. C. Pappas, W. M. S. Wickramanyake, E. Jan, M. Motamedi, M. Brodwick, N. A. Kotov, *Nano Lett.* **2007**, *7*, 513.

[22] H. Bahmani Jalali, M. Mohammadi Aria, U. M. Dikbas, S. Sadeghi, B. Ganesh Kumar, M. Sahin, I. H. Kavakli, C. W. Ow-Yang, S. Nizamoglu, *ACS Nano* **2018**, *12*, 8104.

[23] H. Bahmani Jalali, O. Karatum, R. Melikov, U. M. Dikbas, S. Sadeghi, E. Yildiz, I. B. Dogru, G. Ozgun Eren, C. Ergun, A. Sahin, I. H. Kavakli, S. Nizamoglu, *Nano Lett.* **2019**, *19*, 5975.

[24] M. Han, H. Bahmani Jalali, E. Yildiz, M. H. Qureshi, A. Şahin, S. Nizamoglu, *Commun. Mater.* **2021**, *2*, 19.

[25] O. Karatum, G. O. Eren, R. Melikov, A. Onal, C. W. Ow-Yang, M. Sahin, S. Nizamoglu, *Sci. Rep.* **2021**, *11*, 1.

[26] C. F. Guimarães, R. Ahmed, A. P. Marques, R. L. Reis, U. Demirci, *Adv. Mater.* **2021**, *33*, 1.

[27] H. Yuk, B. Lu, X. Zhao, *Chem. Soc. Rev.* **2019**, *48*, 1642.

[28] F. Fu, J. Wang, H. Zeng, J. Yu, *ACS Mater. Lett.* **2020**, *2*, 1287.

[29] X. Li, L. He, Y. Li, M. Chao, M. Li, P. Wan, L. Zhang, *ACS Nano* **2021**, *15*, 7765.

[30] Z. W. K. Low, Z. Li, C. Owh, P. L. Chee, E. Ye, D. Kai, D. P. Yang, X. J. Loh, *Small* **2019**, *15*, 1805453.

[31] M. Choi, J. W. Choi, S. Kim, S. Nizamoglu, S. K. Hahn, S. H. Yun, *Nat. Photonics* **2013**, *7*, 987.

[32] N. Gogurla, B. Roy, K. Min, J. Y. Park, S. Kim, *Adv. Mater. Technol.* **2020**, *5*, 1900936.

This article is protected by copyright. All rights reserved.

Accepted Article

[33] S. B. Srivastava, R. Melikov, M. M. Aria, U. M. Dikbas, I. H. Kavakali, S. Nizamoglu, *Phys. Rev. Appl.* **2019**, *11*, 12.

[34] N. Martino, P. Feyen, M. Porro, C. Bossio, E. Zucchetti, D. Ghezzi, F. Benfenati, G. Lanzani, M. R. Antognazza, *Sci. Rep.* **2015**, *5*, 1.

[35] B. Lu, H. Yuk, S. Lin, N. Jian, K. Qu, J. Xu, X. Zhao, *Nat. Commun.* **2019**, *10*, DOI 10.1038/s41467-019-09003-5.

[36] A. M. Handorf, Y. Zhou, M. A. Halanski, W. J. Li, *Organogenesis* **2015**, *11*, 1.

[37] B. Yao, H. Wang, Q. Zhou, M. Wu, M. Zhang, C. Li, G. Shi, *Adv. Mater.* **2017**, *29*, 1.

[38] C. Boehler, S. Carli, L. Fadiga, T. Stieglitz, M. Asplund, *Nat. Protoc.* **2020**, *15*, 3557.

[39] C. Dagdeviren, S. W. Hwang, Y. Su, S. Kim, H. Cheng, O. Gur, R. Haney, F. G. Omenetto, Y. Huang, J. A. Rogers, *Small* **2013**, *9*, 3398.

[40] M. Berggren, A. Richter-Dahlfors, *Adv. Mater.* **2007**, *19*, 3201.

[41] M. ElMahmoudy, S. Inal, A. Charrier, I. Uguz, G. G. Malliaras, S. Sanaur, *Macromol. Mater. Eng.* **2017**, *302*, 1600497.

[42] H. Shi, C. Liu, Q. Jiang, J. Xu, *Adv. Electron. Mater.* **2015**, *1*, 1500017.

[43] V. Đerek, D. Rand, L. Migliaccio, Y. Hanein, E. D. Głowacki, *Front. Bioeng. Biotechnol.* **2020**, *8*, 1.

[44] S. B. Baumann, D. R. Wozny, S. K. Kelly, F. M. Meno, *IEEE Trans. Biomed. Eng.* **1997**, *44*, 220.

[45] S. F. Cogan, *Annu. Rev. Biomed. Eng.* **2008**, *10*, 275.

[46] O. S. Abdullaeva, F. Balzer, M. Schulz, J. Parisi, A. Lützen, K. Dedek, M. Schiek, *Adv. Funct. Mater.* **2019**, *29*, 1805177.

[47] M. Jakešová, M. Silverå Ejneby, V. Đerek, T. Schmidt, M. Gryszel, J. Brask, R. Schindl, D. T. Simon, M. Berggren, F. Elinder, E. D. Głowacki, *Sci. Adv.* **2019**, *5*, eaav5265.

[48] E. M. Thaning, M. L. M. Asplund, T. A. Nyberg, O. W. Inganäs, H. Von Holst, *J. Biomed. Mater. Res. - Part B Appl. Biomater.* **2010**, *93*, 407.

[49] P. Takmakov, K. Ruda, K. Scott Phillips, I. S. Isayeva, V. Krauthamer, C. G. Welle, *J. Neural Eng.* **2015**, *12*, 26003.

[50] M. G. Street, C. G. Welle, P. A. Takmakov, *Rev. Sci. Instrum.* **2018**, *89*, 94301.

[51] D. F. Williams, *Annu. Rev. Mater. Sci.* **1976**, *6*, 237.

This article is protected by copyright. All rights reserved.

Accepted Article

[52] Y. Cui, X. Li, K. Zeljic, S. Shan, Z. Qiu, Z. Wang, *ACS Appl. Mater. Interfaces* **2019**, *11*, 38190.

[53] S. Zhang, Y. Chen, H. Liu, Z. Wang, H. Ling, C. Wang, J. Ni, B. Çelebi-Saltik, X. Wang, X. Meng, H. J. Kim, A. Baidya, S. Ahadian, N. Ashammakhi, M. R. Dokmeci, J. Travas-Sejdic, A. Khademhosseini, *Adv. Mater.* **2020**, *32*, 1.

[54] B. P. Bean, *Nat. Rev. Neurosci.* **2007**, *8*, 451.

[55] M. J. I. Airaghi Leccardi, N. A. L. Chenais, L. Ferlauto, M. Kawecki, E. G. Zollinger, D. Ghezzi, *Commun. Mater.* **2020**, *1*, DOI 10.1038/s43246-020-0023-4.

[56] F. C. Delori, R. H. Webb, D. H. Sliney, *J. Opt. Soc. Am. A* **2007**, *24*, 1250.

[57] A. Marino, S. Arai, Y. Hou, E. Sinibaldi, M. Pellegrino, Y. T. Chang, B. Mazzolai, V. Mattoli, M. Suzuki, G. Ciofani, *ACS Nano* **2015**, *9*, 7678.

[58] G. H. Lee, H. Moon, H. Kim, G. H. Lee, W. Kwon, S. Yoo, D. Myung, S. H. Yun, Z. Bao, S. K. Hahn, *Nat. Rev. Mater.* **2020**, *5*, 149.

[59] F. B. Ahmad, J. A. Cisewski, A. Miniño, R. N. Anderson, **2020**, *70*, 519.

[60] Z. Liu, B. Wen, L. Cao, S. Zhang, Y. Lei, G. Zhao, L. Chen, J. Wang, Y. Shi, J. Xu, X. Pan, L. Yu, *Adv. Healthc. Mater.* **2020**, *9*, 1901342.

[61] S. M. Kim, N. Kim, Y. Kim, M. S. Baik, M. Yoo, D. Kim, W. J. Lee, D. H. Kang, S. Kim, K. Lee, M. H. Yoon, *NPG Asia Mater.* **2018**, *10*, 255.

[62] U. Nussinovitch, L. Gepstein, *Nat. Biotechnol.* **2015**, *33*, 750.

[63] M. W. Jenkins, A. R. Duke, S. Gu, Y. Doughman, H. J. Chiel, H. Fujioka, M. Watanabe, E. D. Jansen, A. M. Rollins, *Nat. Photonics* **2010**, *4*, 623.

[64] N. I. Smith, Y. Kumamoto, S. Iwanaga, J. Ando, K. Fujita, S. Kawata, *Opt. Express* **2008**, *16*, 8604.

[65] L. Gentemann, S. Kalies, M. Coffee, H. Meyer, T. Ripken, A. Heisterkamp, R. Zweigerdt, D. Heinemann, *Biomed. Opt. Express* **2017**, *8*, 177.

[66] W. S. Kim, S. Hong, M. Gamero, V. Jeevakumar, C. M. Smithhart, T. J. Price, R. D. Palmiter, C. Campos, S. Il Park, *Nat. Commun.* **2021**, *12*, 157.

[67] L. Yue, J. D. Weiland, B. Roska, M. S. Humayun, *Prog. Retin. Eye Res.* **2016**, *53*, 21.

[68] S. Nizamoglu, M. C. Gather, M. Humar, M. Choi, S. Kim, K. S. Kim, S. K. Hahn, G. Scarcelli, M. Randolph, R. W. Redmond, S. H. Yun, *Nat. Commun.* **2016**, *7*, 10374.

[69] M. Berggren, A. Richter-Dahlfors, *Adv. Mater.* **2007**, *19*, 3201.

This article is protected by copyright. All rights reserved.

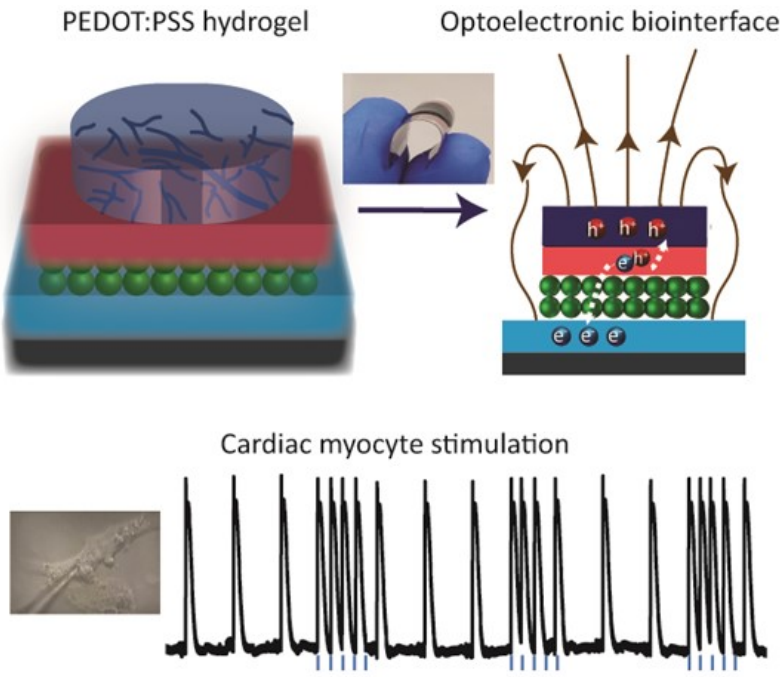
Accepted Article

[70] H. Sirringhaus, T. Kawase, R. H. Friend, T. Shimoda, M. Inbasekaran, W. Wu, E. P. Woo, *Science (80-.).* **2000**, *290*, 2123.

[71] V. R. Feig, H. Tran, M. Lee, K. Liu, Z. Huang, L. Beker, D. G. Mackanic, Z. Bao, *Adv. Mater.* **2019**, *31*, 1902869.

[72] O. Karatum, M. M. Aria, G. O. Eren, E. Yildiz, R. Melikov, S. B. Srivastava, S. Surme, I. B. Dogru, H. Bahmani Jalali, B. Ulgut, A. Sahin, I. H. Kavakli, S. Nizamoglu, *Front. Neurosci.* **2021**, *15*, 724.

ToC Figure



Neural stimulation is a fundamental tool for neurological treatments. Optoelectronic biointerfaces offer unique features with wireless and less-invasive interaction with neurons. Their for-the-first-time integration with hydrogels uniquely brings tissue-like mechanics with boosted capacitive photocurrents for safe and efficient stimulation of neurons. This study additionally shows the great potential of PEDOT:PSS hydrogels for optoelectronic control of beating frequency of cardiac cells.

This article is protected by copyright. All rights reserved.